Check for updates

Phyto-fabrication of ultrafine nanoscale holmium oxide HT-Ho₂O₃ NPs and their biomedical potential

Hamze Elsayed Ahmed Mohamed, [ab] Ali Talha Khalil, [*c] Khaoula Hkiri, [ab] Muhammad Ayaz, [d] Assad Usman, [d] Abdul Sadiq, [d] Farhat Ullah, [d] Ishtiaq Hussain [e] and Malik Maaza [ab]

In this study holmium oxide nanoparticles (Ho₂O₃ NPs) are fabricated using *Hyphaene thebaica* extracts as a bioreductant. The XRD pattern of HT-Ho₂O₃ NPs (product from phyto-reduction) suggested that the nanoparticles are crystalline with no impurities. Scherrer approximation revealed grain sizes of ∼10 nm. The HR-TEM revealed HT-Ho₂O₃ NPs possessed a quasi-spherical morphology complemented by SEM and the particle sizes were in the range of 6–12 nm. The infrared spectra revealed characteristic Ho–O bonding at ∼603 cm⁻¹. Raman spectra indicated five main peaks positioned at 156 cm⁻¹, 214 cm⁻¹, 328 cm⁻¹, 379 cm⁻¹ and 607 cm⁻¹. E_g (optical bandgap) was found to be 5.1 eV. PL spectra indicated two major peaks at 415 nm and 607 nm. EDS spectra confirmed the elemental presence of holmium (Ho). Spotty rings were obtained during the SAED measurement which indicated crystallinity of HT-Ho₂O₃ NPs. The HT-Ho₂O₃ NPs were further analyzed for their antioxidant, anti-angiogenic and cytotoxic properties. The antioxidant potential was moderate *i.e.*, 43.40 ± 0.96% at 1000 μg mL⁻¹ which decreased in a dose dependent manner. Brine shrimp lethality was highest at 1000 μg mL⁻¹ with the LC₅₀ 320.4 μg mL⁻¹. Moderate anti-angiogenic potential was observed using *in ova* CAM assay. MTT bioassay revealed that the HT-Ho₂O₃ NPs inhibited the 3T3 cells (IC₅₀ 67.9 μg mL⁻¹), however, no significant inhibition was observed against MCF-7 cells. α-Amylase and β-glucosidase inhibition revealed that the HT-Ho₂O₃ NPs can be of use in controlling blood glucose levels. Overall, it can be concluded that biosynthesis using aqueous extracts can be a suitable alternative in finding ecofriendly paradigms for the synthesis of nanoparticles. We suggest extended research into the bioreduced Ho₂O₃ NPs for establishing their biomedical potential and toxicity.

1. Introduction

Rare earth oxide materials (REMs) such as holmium oxide (Ho₂O₃) are known for their interesting physicochemical, optical, magnetic, electrical and biological properties. Like other sesqui-oxides, Ho₂O₃ is used in various applications including optical applications such as calibration of the wavelength in instruments, pyrolysis, catalysis, electrochemical sensing, memory devices *etc.*[1-3] The basic and catalytic properties of Ho₂O₃ are reliant on the fabrication methods.[4] In the REMs, Ho₂O₃ NPs are known for elevated lattice energy and a large magnetic moment. Under normal conditions, Ho₂O₃ has a bixbyite or cubic structure up to 2200 °C, however, at elevated pressures it shows polymorphic monoclinic transformation.[5] Ho₂O₃ NPs supported on MCN have indicated promising applications in radiation therapy.[6] Ho₂O₃ NPs have been previously explored for the photocatalytic degradation of various environmental contaminants.[7-9] In medical sciences, the holmium-based lasers are widely used for lithotripsy. Laser energy released from Holmium: YAG is efficiently absorbed in aqueous environments and thus has no side effects like delayed tissue necrosis.[10] Neutron-activatable Holmium based materials have been widely applied in the therapeutic radionuclide targeting of tumor cells in systemic radiation therapy.[6,11]

Various physicochemical processes are suggested for synthesis of Ho₂O₃ NPs of. These wet chemical and physical approaches includes chemical bath deposition, gel diffusion method, thermal decomposition, sono-chemical, solvothermal hydro-thermal methods.[1,2] Thermal decomposition of different precursors like Ho(NO₃)₃·5H₂O and Ho₂(OH)₂(CO₃) have been reported for the synthesis Ho₂O₃ NPs.[12-14] Despite of showing effectiveness these physical and chemical processes possess limitations. It is well recognized that the chemical processes can produce noxious waste and are non-biocompatible due to residual chemical

ᵃUNESCO UNISA Africa Chair in Nanoscience and Nanotechnology, College of Graduate Studies, University of South Africa, Pretoria, South Africa

ᵇNanoscience African Network (NANOAFNET), Materials Research Department, iThemba LABS, Cape Town, South Africa. E-mail: khawlahkiri24@gmail.com

ᶜDepartment of Pathology, Lady Reading Hospital Medical Teaching Institution, Peshawar, 25000 KP, Pakistan. E-mail: alitalha.khalil@lrh.edu.pk

ᵈDepartment of Pharmacy, Faculty of biological sciences, University of Malakand, Chakdara 18000, Dir (L), KPK, Pakistan. E-mail: ayazuop@gmail.com; assadrph@gmail.com; farhataziz80@hotmail.com

ᵉDepartment of Pharmaceutical sciences Pak Austria fachhachole Mang haripur, Pakistan. E-mail: ishtiaqdr025@gmail.com

precursors which compromises their applications in medicine. Whereas, the physical processes are costly because of their energy needs and sophisticated requirements.[15,16] In recent years the plant extracts-based fabrication of metal nanoparticles has emerged as an ecofriendly and economical paradigm.[15,17] The nano-bio interface has brought stimulating results and the bio-
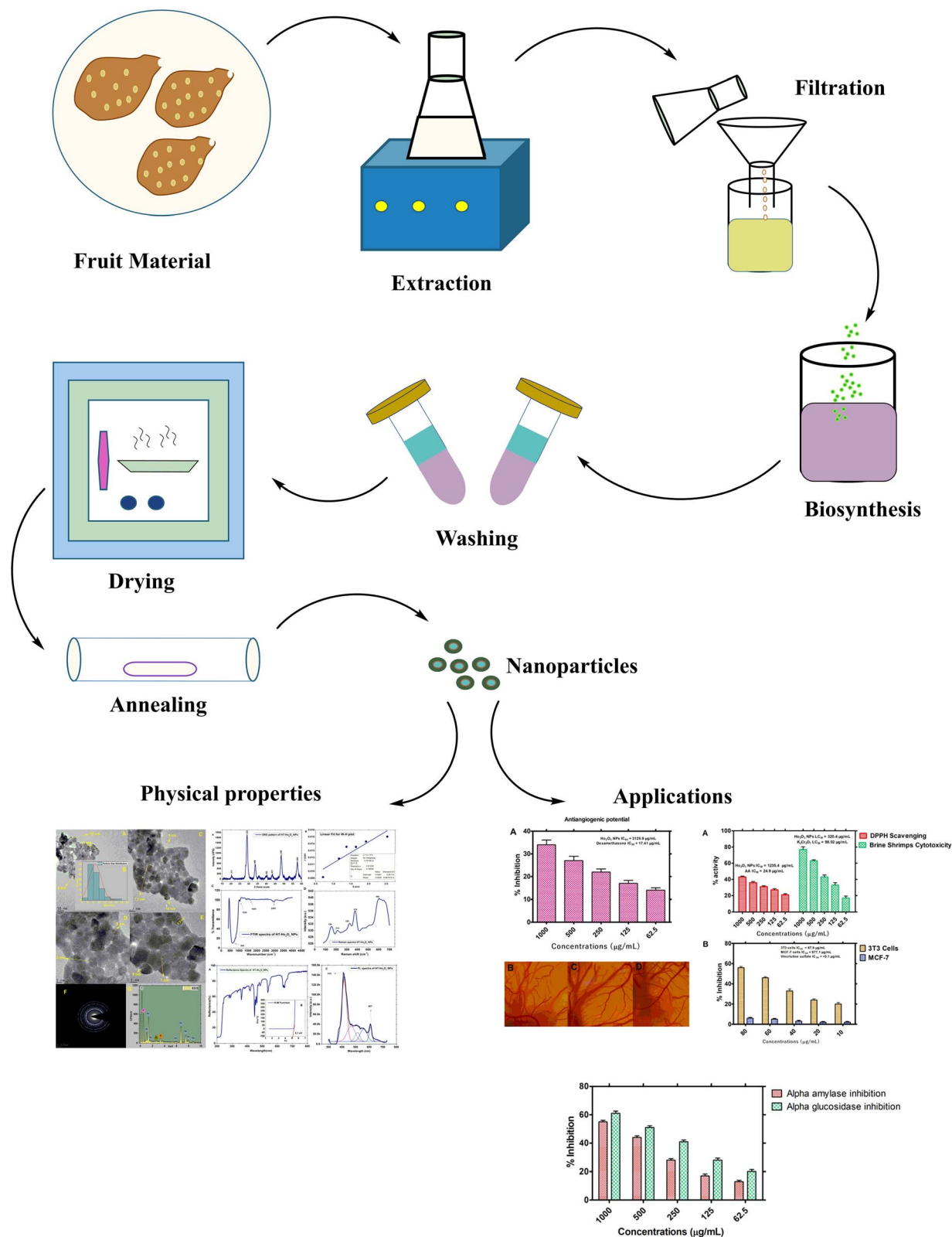

Fig. 1 Study scheme.

fabrication of multifunctional metal-based nanoparticles (NPs) with appealing properties represents a trending area in material sciences.[18] The abundance and diversity of the natural resources have shifted the thrust towards green chemistry-based synthesis of the nanoparticles.[16] Various metal nanoparticles or composite nanomaterials have been fabricated using plant extracts. The nanoparticles reported through the bioreduction process are often reported to have high compatibility and effectiveness as compared to the nanoparticles synthesized from other routes. Generally, the phyto-fabrication is a simple one step process catalyzed by phytochemicals which plays a dual role of reducing the precursor metal salt and subsequently capping for their stabilization of the nanoparticles.

As much of the attention in phyto-reduction based synthesis of metal nanoparticles is centered on silver and gold nanoparticles and there is no report on the phyto-reduction route for the synthesis of Ho_2O_3 nanoparticles. We for the 1st time successfully report phyto-reduction based synthesis of Ho_2O_3 nanoparticles using fruit extracts of *Hyphaene thebaica* as chelating and capping agents. *H. thebaica* is also known as Egyptian doum and has been reported for diverse medicinal uses in folkloric medicines. Previously, we have successfully fabricated nanoparticles of silver, ceria, iron oxide, bismuth vanadate, zinc oxide, chromium oxide, lanthanum oxide, erbium oxide, europium oxide[19–24] using *H. thebaica* and further evaluated their biomedical potential. Herein, the structural, optical vibrational and functional properties of HT-Ho_2O_3 NPs (product from phyto-reduction) are reported. Later the HT-Ho_2O_3 NPs were evaluated for anticancer, antiangiogenic, cytotoxic, antioxidant potential. The study scheme of the current study is indicated in Fig. 1.

2. Experimental

2.1. Plant material collection and identification

The plant material was collected in Aswan (Egypt) and the taxonomic identification was done by Dr E. Ammar by comparing it with the already available voucher specimen "29 469" in herbarium, Aswan Botanical Garden, Aswan, Egypt. The plant *H. thebaica* is commonly available in Egypt and its not a threatened or endangered species. *H. thebaica* fruits are commonly available in egyptian markets and can also be purchased. The fruit material was rinsed in distil water and dried in shade which followed by grounding them to powder and finally stored in zipper bags. 10 g powdered material was added to dH_2O (200 mL), heated for 2 h at 80 °C on a magnetic hotplate. Obtained aqueous extracts were filtered to remove leftover material and the optically transparent liquid extracts were used for further experiments.[25]

2.2. Biosynthesis of HT-Ho_2O_3 NPs

For biosynthesis of HT-Ho_2O_3 NPs, the 100 mL aqueous extracts were treated with 3.5 g precursor salt *i.e.*, holmium nitrate and the reaction mix was heated for 2 h at 60 °C and cooled to room temperature, centrifuged at 5000 RPM for 15 min for collecting the precipitates which were washed thrice in distil water at 5000 RPM. Finally, the precipitates kept in oven at 70 °C for 2 h for drying and later kept in the glass tube furnace for 2 h at 500 °C for annealing.[26] The annealed powder assumed as HT-Ho_2O_3 NPs were used for characterization.

2.3. HT-Ho_2O_3 NPs characterization

Room temperature X-ray diffraction pattern was obtained to obtain the structural properties of HT-Ho_2O_3 NPs. The spectral data was used to calculate major XRD values (Table 1). Debye Scherrer approximation (eqn (1)) and W–H plot method (eqn (2)) were applied for the crystallite size estimation. Dislocation density was determined (eqn (3)). FTIR spectra and Raman spectra was used to identify the functional and vibrational characteristics of HT-Ho_2O_3 NPs. Optical properties were established by diffuse reflectance and photoluminescence spectra. Bandgap was calculating from reflectance by applying K–M function (eqn (4) and (5)). Nanoparticles shape and morphology was observed using HR-TEM and SEM. Image J was used for the processing of the HR-TEM images and calculation of the particle size distribution. Elemental composition was identified by EDS spectra and the SAED pattern was obtained. After establishing the room temperature properties of HT-Ho_2O_3 NPs, they were subjected to extensive investigations for assessing their biomedical potential.[27]

$$\langle D \rangle_{size} = \frac{K\lambda}{\Delta\theta_{\frac{1}{2}}} \cos\theta \qquad (1)$$

whereas "λ" denote the Cu-Kα radiation X-ray wavelength (1.54 Å), and "K" represents Scherrer constant (0.9), "θ" is the Bragg angle and "β" is the FWHM and "D" represents the crystallite size.

$$\beta\cos\theta = \frac{(K\lambda)}{D} + 4\varepsilon\sin\theta \qquad (2)$$

Table 1 Major calculations from XRD data

Miller indices (*hkl*)	2θ	FWHM-β	D (nm)	Dislokasyon-δ	Strain-ε
211	20.41481	0.51883	14.89634	0.004506515	0.002228
222	29.07565	0.84919	8.9515	0.01247982	0.003587
400	33.71933	0.70524	10.65655	0.008805762	0.002945
332	40.12402	0.80642	9.147165	0.011951625	0.003305
431	43.37143	0.63955	11.40984	0.007681407	0.002593
440	48.44382	0.84803	8.444997	0.01402171	0.003374
622	57.56025	0.92962	7.404007	0.018241745	0.003555
Average			10.13006	0.011098369	0.003084

Paper

On the x-axis, $\beta \cos \theta$ was plotted against $4 \sin \theta$ followed by obtaining a linear fit for obtaining the y-intercept and strain (ε) for calculating the crystallite size (D) by W–H method.[28] Dislocation density "δ" was obtained by eqn (3);[29]

$$\delta = \frac{1}{D^2} \qquad (3)$$

Optical band gap was obtained using Kubelka–Munk function using eqn (4) and (5). Here, "R" is the diffused reflectance and "$F(R)$" is the K–M function.[22]

$$F(R) = \frac{(1-R)^2}{2R} \qquad (4)$$

$$F(R)h\nu = A(h\nu - E_g)^n \qquad (5)$$

2.4. *In vitro* FRSA potential

FRSA (Free Radical Scavenging) of HT-Ho$_2$O$_3$ NPs was investigated using DPPH assay.[30,31] The DPPH reagent solution (0.004%) was prepared in methanol. Different serial dilutions (62.5 μg mL^{-1} to 1000 μg mL^{-1}) of HT-Ho$_2$O$_3$ NPs were prepared in distil water, from which 0.1 mL was treated with 3 mL free radical's solution. The reaction mix was incubated in the dark for 30 min. Finally, the readings were recorded at 517 nm by UV spectrophotometer. Ascorbic acid was taken as a positive control in the assay. Percent free radical scavenging was obtained using the following equation;

$$\text{percent inhibition} = \frac{\text{abs. ct} - \text{abs. sp}}{\text{abs. ct}} \times 100 \qquad (6)$$

whereas the abs. ct is the absorbance by control and abs. sp was absorbance shown by the test sample.

2.5. *In vitro* brine shrimp lethality

Brine shrimps or *Artemia salina* were used in the investigation of the cytotoxic properties of HT-Ho$_2$O$_3$ NPs.[32] Artificial sea water (ASW) was used for hatching the larvae. The preparation of ASW included sea salt (40 g) in 1 L distilled water. Shrimps' eggs (2 g) were introduced to the ASW and suspended using an air pump. The container was incubated for 48 h in a warm condition for hatching with a light source on top. Hatched larvae (10 in number) were collected in a separate container and transferred to microplate, which was pre-treated with triplicate serial dilutions (62.5 μg mL^{-1} to 1000 μg mL^{-1}) of HT-Ho$_2$O$_3$ NPs, followed by incubation for 24 h. After incubation, live and dead larvae were counted for calculation of percent cytotoxicity and LC$_{50}$. For positive control, Potassium dichromate was applied.

2.6. *In ovo* antiangiogenic assay

The antiangiogenic properties of HT-Ho$_2$O$_3$ NPs were studied using chorioallantoic membrane assay (CAM).[33] Briefly, after incubating fertilized eggs for 4 days incubation at 37 °C the location of embryo was identified followed by removal of 1 mL albumin. Under aseptic conditions, the CAM surface was accessed by creating a small opening. HT-Ho$_2$O$_3$ NPs serial dilutions (62.5 μg mL^{-1} to 1000 μg mL^{-1}) were prepared in normal saline and applied to the CAM surface by a filter paper disc. For positive and negative controls dexamethasone and normal saline were used respectively. After application of the test samples, the opening was properly sealed and incubated for 48 hours. The antiangiogenic properties were established by counting the blood vessels using the below formula;

$$\text{percent inhibition} = \frac{\text{CAMn} - \text{CAMs}}{\text{CAMn}} \times 100 \qquad (7)$$

whereas; "CAMn" is number of blood vessels in CAM treated with normal saline and "CAMs" is blood vessels number in CAM treated with HT-Ho$_2$O$_3$ NPs.

2.7. MTT assay

The MTT (3-(4,5-dimethylthiazolyl-2)-2,5-diphenyltetrazolium bromide) assay for HT-Ho$_2$O$_3$ NPs were performed on MCF-7 and 3T3 cell lines.[34,35] Dulbecco's Modified Eagle Medium (DMEM) medium was used for culturing cell lines in microplate. DMEM was supplemented with streptomycin and penicillin at 50 units per mL each and FBS (10%). The cultures were grown up to the density of 6×10^4 cells per well and incubated with different concentration of HT-Ho$_2$O$_3$ NPs after replacing with fresh DMEM media, and kept for 24 h. 20 μL MTT reagent prepared in PBS was added to each well and followed by incubation for 4 h at 37 °C. Finally, DMSO (200 μL) was introduced which dissolved the formazan crystals and the readings were taken at 570 nm. Cellular viability was obtained using eqn (8).

$$\text{percent cell viability} = \frac{\text{test sample absorbance}}{\text{negative control absorbance}} \times 100 \qquad (8)$$

2.8. Alpha glucosidase inhibitory assay

Previously described procedure was applied to assess the inhibitory properties of HT-Ho$_2$O$_3$ NPs α-glucosidase enzyme.[36] For obtaining the reagent solution the α-glucosidase enzyme (0.5 μg mL^{-1}) was introduced to 120 μL of phosphate buffer (pH 6.9). Serial dilutions of the test sample (1000–62.5 μg mL^{-1}) were prepared. The reagent solution and the serial dilutions were treated initially for 20 min and kept at 37 °C. Afterwards, substrate solution (20 μL) was introduced to reaction mix and incubated for 15 min at 37 °C. Finally, Na$_2$O$_3$ solution (80 μL) was introduced and the absorbance taken at 405 nm. Acarbose was taken as a positive control and a blank mixture without inhibitor agents was used as a negative control. Eqn (9) was applied for calculating the % α-glucosidase inhibition.

$$\% \text{ inhibition} = \frac{\text{control absorbance} - \text{test sample absorbance}}{\text{control absorbance}} \times 100 \qquad (9)$$

2.9. Alpha-amylase inhibitory assay

Alpha-amylase enzyme inhibitory effect of the HT-Ho2O3 NPs was performed as described previously.[37] Briefly, a 20 μL alpha-amylase and 200 μL from the 0.02 M sodium phosphate buffer

was introduced to different concentrations (1000–62.5 μg mL−1) of the test sample, followed by incubation for 10 min at room temperature. The reaction mixture was further added with starch (200 μL) and 400 μL of DNS (dinitrosalicylic acid) reagent and incubated for 5 minutes in a water bath. Finally, 15 mL of double-distilled water was introduced to the mixture and absorbance was recorded at 540 nm. Acarbose taken as a standard α-amylase inhibitor and the percent inhibitory effect was calculated using the formula.

$$\% \text{ inhibition} = \frac{\text{control absorbance} - \text{test sample absorbance}}{\text{control absorbance}} \times 100$$

(10)

3. Results

3.1. Physical properties

3.1.1. Structural properties. Multiple procedures were applied to establish the properties of HT-Ho$_2$O$_3$ NPs. The inset Fig. 2A indicate the XRD pattern of HT-Ho$_2$O$_3$ NPs which suggest that the HT-Ho$_2$O$_3$ NPs were crystalline with no impurities. The obtained Bragg peaks were centered as 20°, 29°, 33°, 39°, 43°, 48° and 57° are ascribed to the crystallographic reflections from (211), (222), (400), (332), (431), (440) and (622) respectively. The observed Bragg peaks corelated to the JCPDS Pattern 044-1268 belonging to the body centered cubic Ho$_2$O$_3$ and space group $Ia\bar{3}$. Lattice constants were deduced as $\langle a_{exp}\rangle = 10.61$ Å and $\langle z_{exp}\rangle = 16$ Å. The crystalline size determined by the Debye–Scherrer equation by using the diffraction data was found to be 10 nm. Major XRD values are summarized in Table 1. For further identifying the crystallite size, the Williamson–Hall equation was used which revealed crystallite size of 17.2 nm. Fig. 2B shows the linear fit after plotting $\beta \cos\theta$ and 4 $\sin\theta$ for obtaining y-intercept and strain. Strain was calculated as 0.003. The Debye Scherrer approximation revealed an average crystallite size of ~10 nm.

3.1.2. Vibrational properties. The vibrational and functional features of the HT-Ho$_2$O$_3$ NPs were established by FTIR and Raman spectra as shown in Fig. 2C and D respectively. FTIR spectra reveals vibrations centered at ~603 cm^{-1}, 1050 cm^{-1}, 1625 cm^{-1} and 2995 cm^{-1}. The intense vibration positioned at ~603 cm^{-1} can be ascribed to the traditional metal and oxygen bonding *i.e.*, Ho–O.[38] Small peaks located at 1050 cm^{-1} and
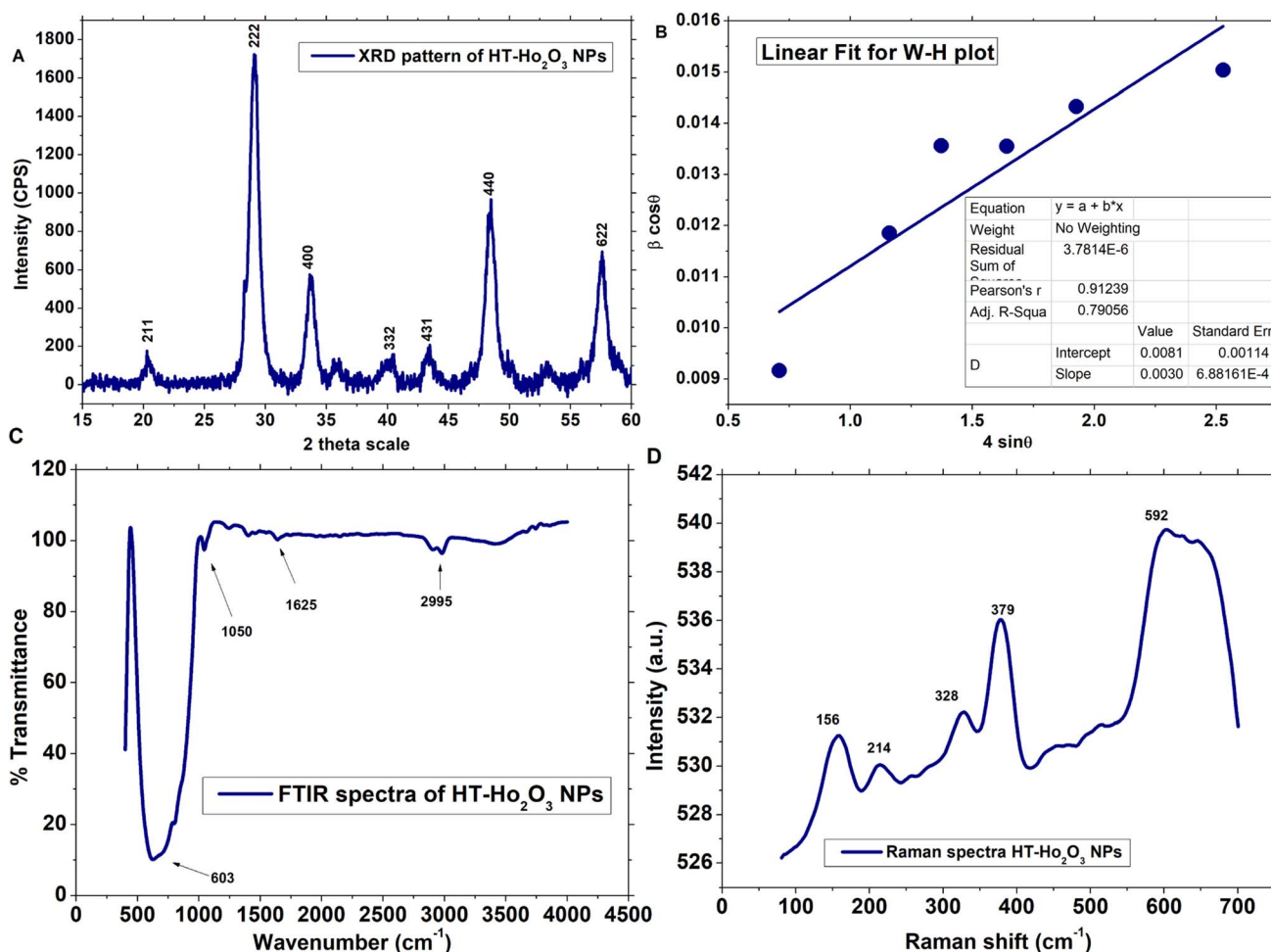

Fig. 2 Structural and functional characterization of the HT-Ho$_2$O$_3$ NPs; (A) XRD pattern (B) W−H plot; (C) FTIR; (D) Raman spectrum.

$1625\ cm^{-1}$ can be ascribed to the carbonyl (C=O) and alkenes (C=C) functional group. Fig. 1D reveals the Raman spectra HT-Ho_2O_3 NPs which indicates five distinct peaks positioned at $156\ cm^{-1}$, $214\ cm^{-1}$, $328\ cm^{-1}$, $379\ cm^{-1}$ and $590\ cm^{-1}$ respectively. Generally, the Raman spectra of the rare earth oxide materials is often complex and depend on the excitation wavelength, while it may include PL signals from the metal ions. The intensive Raman peak for rare earth oxide materials is usually observed in the region of $320–420\ cm^{-1}$. A strong peak at $\sim379\ cm^{-1}$ ($F_g + A_g$) is the indicative of the well-crystalline Ho_2O_3 NPs.[12,39] Vibration modes at $\sim156\ cm^{-1}$, $\sim328\ cm^{-1}$ and $\sim590\ cm^{-1}$ are also previously reported.[39,40]

3.1.3. Optical properties. The optical properties of HT-Ho_2O_3 NPs were established using DRS and PL spectra as indicated in inset Fig. 3A–C. The DRS was analyzed by K-M function for the determination of the optical bandgap (E_g) which was calculated as 5.1 eV which is well agreed in the literature and can be attributed to the blue shift due to decrease in the size.[2] Other authors have reported E_g values of 3.2 eV,[7] 4.95 eV,[1] 5.0 eV (ref. 41) etc. The PL spectra of the HT-Ho_2O_3 NPs is indicated in Fig. 2C revealing two major emission peaks at 415 nm and a relatively less intense peak at 607 nm reflects electronic transition from ground state of $^5I_8$ to $^5G_5$ and $^5F_5$ $^5I_8 \rightarrow {}^5G_5$ for 415 nm and $^5I_8 \rightarrow {}^5F_5$.

3.1.4. Surface morphology and composition. HT-Ho_2O_3 NPs morphology was established using HR-TEM as indicated in the inset Fig. 4A, C and D. The nanoparticles were having spherical to cuboidal shapes with most of the nanoparticles were in the range of 6–10 nm as indicated in Fig. 4B. Selected area electron diffraction pattern revealed spotty circular rings which reflects the crystalline nature of the HT-Ho_2O_3 NPs. The energy dispersive spectra confirmed the presence of holmium and oxygen. In the EDS spectra other peaks i.e., carbon and potassium. Presence of carbon is attributed to which carbon

coated grid whereas the elemental presence of potassium can be ascribed to the plant material. SEM images were acquired to study the surface morphology of the nanoparticles which showed that the nanoparticles were mostly spherical in shape. The SEM images are indicated in Fig. 5A and B.

3.2. Biomedical potentials

3.2.1. _In vitro_ antioxidant and cytotoxic properties. It was observed that the free radical potential of the HT-Ho_2O_3 NPs was dose responsive. Visual observation indicated slight changes in the purple color of the DPPH reagent, reflecting their moderate free radical scavenging potential. From the absorbance values the percentage radical scavenging were calculated. At different tested concentrations of 62.5, 125, 250, 500 and 1000 μg mL^{-1}, the percent inhibition was $21 \pm 1.37\%$, $27.43 \pm 1.50\%$, $31.30 \pm 1.17\%$, $36.31 \pm 1.43\%$ and $43.40 \pm 0.96\%$ respectively, as shown in Fig. 6A. An IC_{50} value of 1235.4 μg mL^{-1} was obtained which was significantly less as compared to the ascorbic acid (IC_{50}: 24.9 μg mL^{-1}). In the brine shrimp cytotoxicity assay, the different concentration HT-Ho_2O_3 NPs were tested on _Artemia salina_ nauplii. HT-Ho_2O_3 NPs revealed a dose dependent cytotoxicity i.e., $17 \pm 2.46\%$, $33.33 \pm 3.05\%$, $43.33 \pm 2.41\%$, $63.33 \pm 1.27\%$ and $76.67 \pm 3.3\%$ at concentration of 62.5, 125, 250, 500 and 1000 μg mL^{-1} respectively, as shown in Fig. 6A. The LC_{50} value of 320.4 μg mL^{-1} was obtained for HT-Ho_2O_3 NPs whereas LC_{50} value 98.02 μg mL^{-1} for the reference potassium dichromate.

3.2.2. Cell culture assays. Anticancer characteristics of HT-Ho_2O_3 NPs was established using MCF-7 and 3T3 cancer cell lines as indicated in Fig. 6B. It was observed that the HT-Ho_2O_3 NPs actively inhibited the 3T3 cells as compared to the MCF-7. At concentration 80 μg mL^{-1}, the HT-Ho_2O_3 NPs revealed cytotoxicity of $56 \pm 1.23\%$ and $6.5 \pm 0.80\%$ for 3T3 and MCF-7 cancer cells. The IC_{50} value for MCF-7 cells was 877.1 μg mL^{-1}

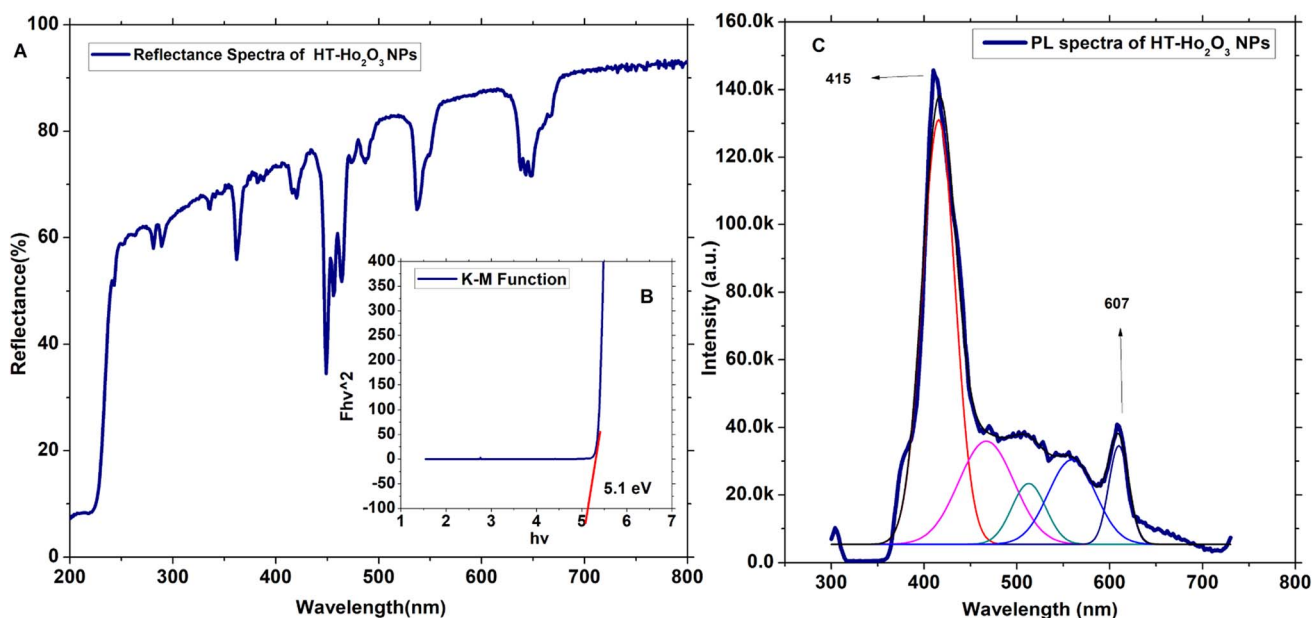**Fig. 3** Optical characteristics of HT-Ho_2O_3 NPs; (A) DRS spectrum; (B) E_g calculation by K–M function; (C) PL spectrum.
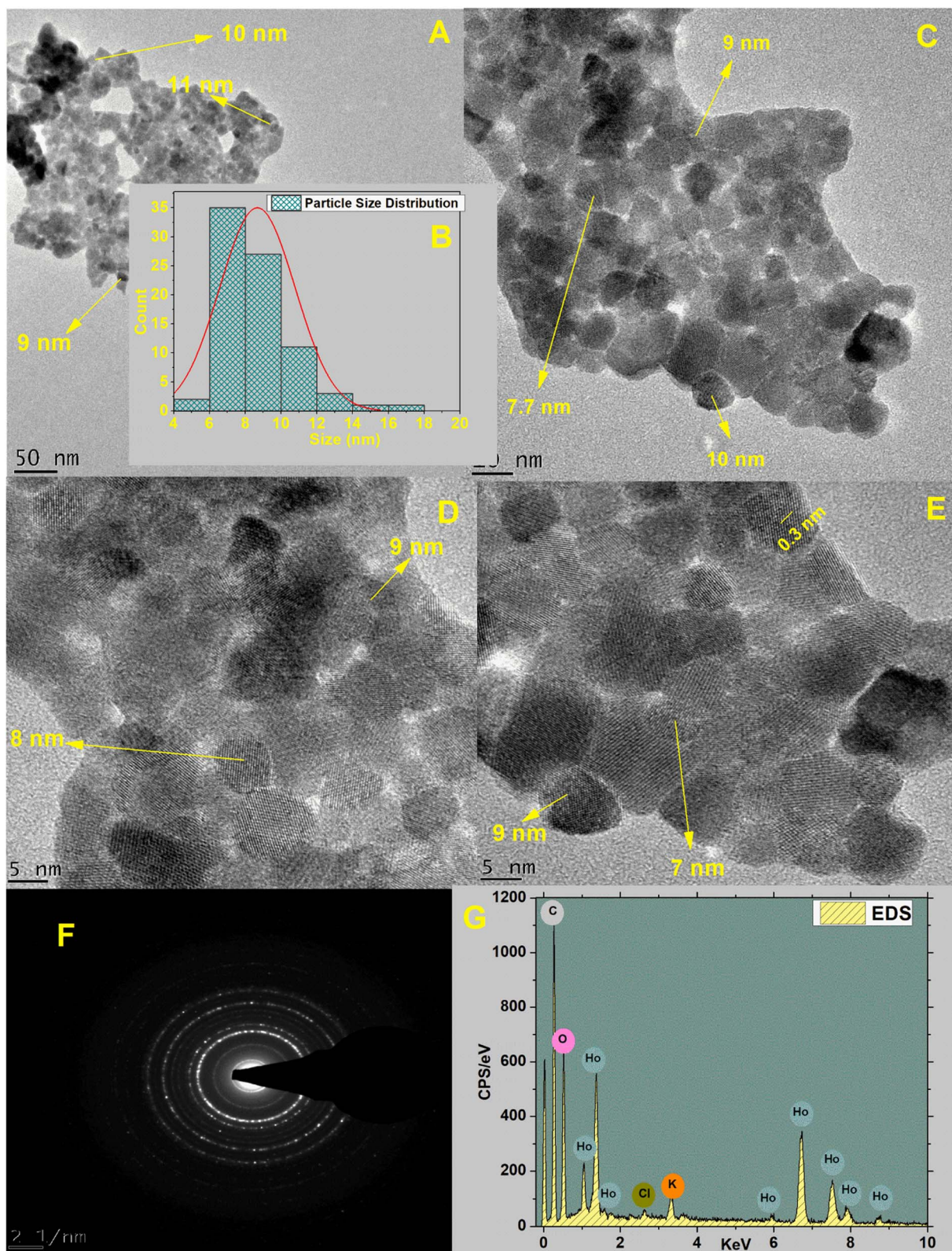
Fig. 4 Various characterization techniques applied on HT-Ho_2O_3 NPs; (A; C; D; E) HRTEM images acquired at changed magnifications; (B) particle size distribution; (F) selected area electron diffraction pattern; (G) EDS spectrum.

while the 3T3 cells show an IC_{50} value of 67.9 μg mL^{-1}. Vincristine sulfate used as a positive control exhibited an IC_{50} value <0.1 μg mL^{-1}. The results are presented in Fig. 6B.

3.2.3. Anti-angiogenic assay. Angiogenesis is a vital step in the development or growth of tumor, therefore, HT-Ho_2O_3 NPs were evaluated for anti-angiogenic potential by CAM assay. For
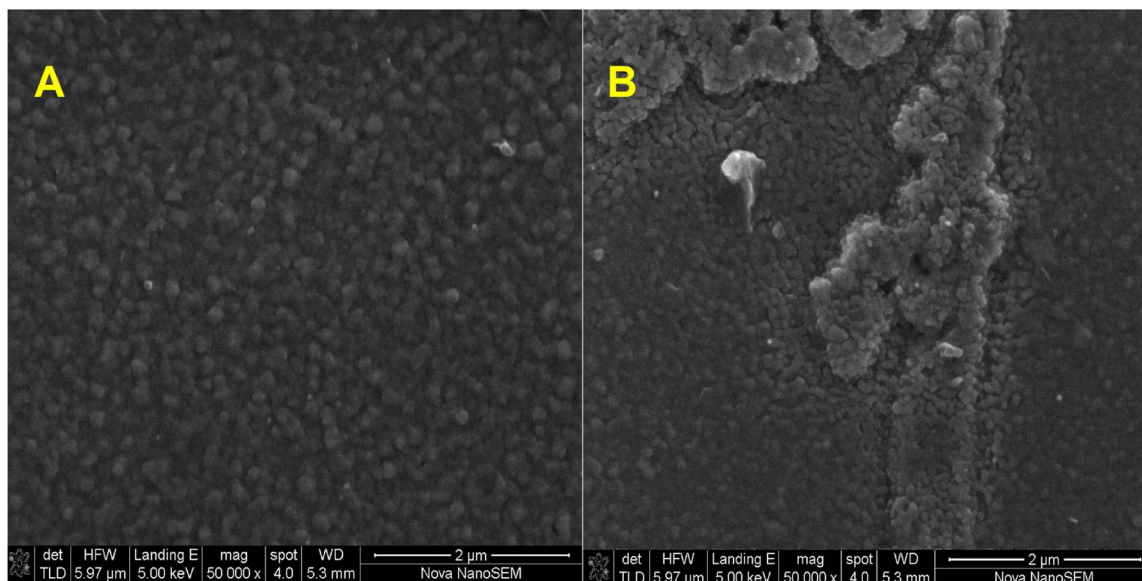
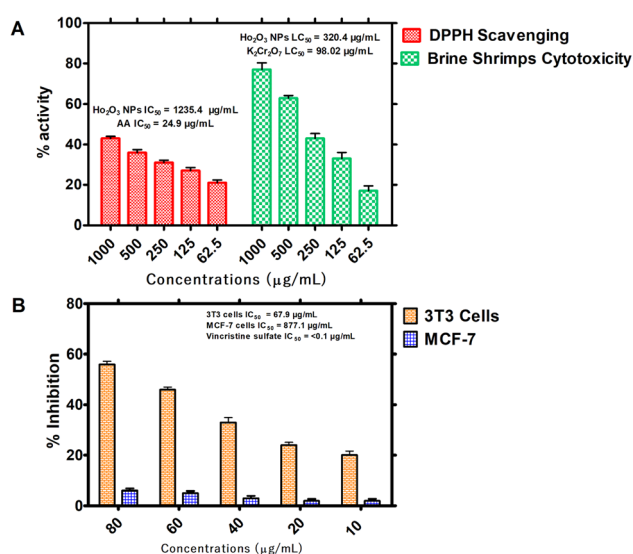**Fig. 5** (A) and (B) SEM images of the HT–Ho_2O_3 NPs.

Fig. 6 *In vitro* bioassays on the HT– Ho_2O_3 NPs; (A) percent free radical scavenging effect at different concentrations and their brine shrimp cytotoxicity potential; (B) the *in vitro* MTT cytotoxicity assay on 3T3 and MCF-7 cells.

α-glucosidase inhibition as indicated in Fig. 8. At different tested concentration *i.e.*, 1000, 500, 250, 125, and 62.5 µg mL^{-1}, the percent α-glucosidase inhibition of 61.32 ± 1.61%, 50.94 ± 1.27%, 40.57 ± 1.19%, 27.99 ± 1.44% and 20.13 ± 1.37% was observed respectively. The IC$_{50}$ value of the nanoparticles was determined to be 467.1 µg mL^{-1} while the positive reference
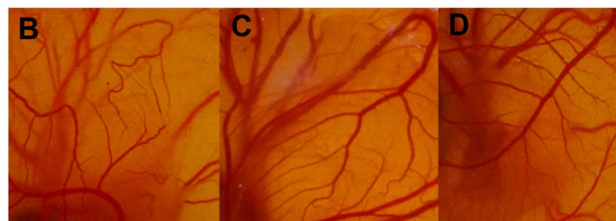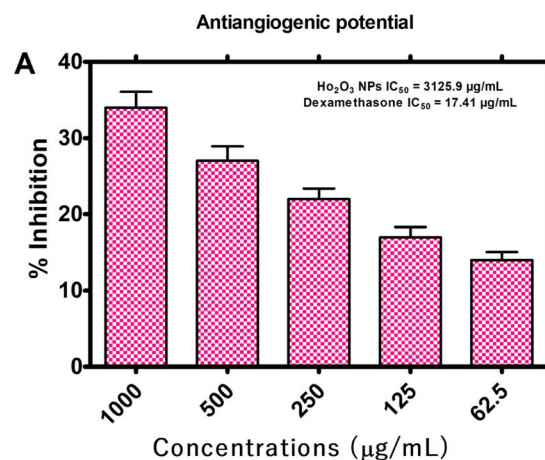

Fig. 7 Antiangiogenic potential of the HT–Ho_2O_3 NPs (A) percent inhibition of angiogenesis in ova at different concentrations; (B–D) selected photos of the *in ovo* CAM bioassay at different concentrations.

this purpose, the reliable and inexpensive in ovo CAM assay was used for assessing the anti-angiogenic potential of HT-Ho_2O_3 NPs. The results are indicated in Fig. 7A–D. Across the tested concentration *i.e.*, 62.5, 125, 250, 500 and 1000 µg mL^{-1} of the HT-Ho_2O_3, the percent inhibition was observed as 3.84 ± 1.05%, 16.96 ± 1.81%, 21.88 ± 1.37%, 27.15 ± 1.92% and 34.41 ± 2.09% respectively. The IC$_{50}$ value calculated for HT-Ho_2O_3 NPs was 3125.9 µg mL^{-1} while the positive control dexamethasone exhibited an IC$_{50}$ value of 17.41 µg mL^{-1}.

3.2.4. Antidiabetic potential. The antidiabetic potential of the HT-Ho_2O_3 NPs was examined through *in vitro* α-amylase and

Fig. 8 Antidiabetic potential of the HT-Ho$_2$O$_3$ NPs.

acarbose exhibited an IC$_{50}$ value of 20.4 μg mL^{-1} in this assay. Similarly, on the same doses, the α-amylase inhibition was observed to be 54.70 ± 1.05%, 44.34 ± 1.14%, 28.19 ± 1.10%, 16.87 ± 1.37% and 13.01 ± 0.91%. The IC$_{50}$ value in the α-amylase inhibition assay was 741 μg mL^{-1} for the HT-Ho$_2$O$_3$ NPs and 36.6 μg mL^{-1} for acarbose which was used as positive control.

4. Discussion

Bio-fabrication of the nanomaterials owes several advantages over other physical and chemical means. These includes their sustainable nature, easiness of the process and enhanced compatibility. Plants constitute of diverse secondary metabolites that possesses different pharmacological properties and also has potential to reduce bulk metals into their ions. Such bioactive molecules act as green reducing and stabilizing agents.[42–44] The therapeutic potential of the fruits of *H. thebaica* is well established. Previously, we have reported *H. thebaica* mediated synthesis of Fe$_2$O$_3$ (ref. 22), CeO$_2$ (ref. 21), Cr$_2$O$_3$ (ref. 23), BiVO$_4$,[45] ZnO,[46] CuO,[47] Er$_2$O$_3$ (ref. 48) and Ag nanoparticles [20]. The biosynthesis of holmium oxide nanoparticles is reported for the 1st time. The plant *H. thebaica* possesses a rich phytochemistry which constitutes different organic acids and other components like naringin, quercetin, glycosides, tannins, saponins *etc.* are also reported in the *H. thebaica*.[49,50] These plant constituents have the capacity to catalyze redox reactions and stabilize the nanoparticles.[51] XRD pattern was consistent with previous reports.[52] Similarly, the FTIR spectrum revealed a characteristic metal oxide vibration at ∼603 cm^{-1}. "E_g" was calculated as 5.1 eV which is in agreement with previous reports.[2] The biomedical applications of the holmium oxide nanoparticles are not exclusively covered in the literature.

We have reported for the 1st time the anticancer and antidiabetic potential of biogenic HT-Ho$_2$O$_3$ NPs. The anticancer applications revealed that the nanoparticles exhibited toxicity against 3T3 cell lines while insignificant anticancer potential was observed on MCF-7 cell lines. The anticancer properties of holmium-based materials have been reported. For example, the holmium ferrite nanoparticles coated with cyclodextrin and polyethylene glycol loaded with camptothecin, an anticancer drug revealed anticancer potential 79.42% when tested at 250 μg mL^{-1}.[53] A similar nanocarrier system based on holmium ferrite was described for the potential treatment of human

glioma cancer.[54] The anticancer mechanism of the rare earth lanthanides is mostly ascribed to the oxidative stress generated by the reactive oxygen species, retarding the calcium transport, direct interaction with cellular organelle and DNA, endoplasmic reticulum stress, activating the mitogen-activated protein kinase (MAPK) *etc.*[55–57] One of the key aspects of the cancer progression is the formation of new vasculature *i.e.*, angiogenesis which facilitate the influx of nutrients to the cancer cells for keeping them alive.[58] Keeping in view, we have tested the HT-Ho$_2$O$_3$ NPs through in ovo CAM assay which is routinely performed for the assessment of inhibition of angiogenesis. Our results clearly indicate that the HT-Ho$_2$O$_3$ NPs can have applications in the inhibition of angiogenesis.

Furthermore, we have evaluated the antidiabetic potential of the as fabricated HT-Ho$_2$O$_3$ NPs. One of the popular strategies to control postprandial levels of glucose in the body relates to the inhibition of the enzymes that actively breakdown the carbohydrates into glucose and raise their levels in the body. Hence, the diabetic treatment research revolves around the effective α-amylase and α-glucosidase inhibitors. These enzymes tends to facilitate the breakdown of complex carbohydrates to glucose and their inhibition reduces glucose absorption in the intestine.[59] We have shown that the HT-Ho$_2$O$_3$ NPs possesses the ability to inhibit the α-amylase and α-glucosidase enzymes.

The chemical and physical means of synthesis of the nanoparticles possess disadvantages like generating hazardous waste and being expensive, whereas plant extracts-based synthesis is embodying the principals of green chemistry provides a cost effective and green alternative for the synthesis of the metal nanoparticles. Among biological resources, plants are mostly preferred for the biosynthesis of nanoparticles as they have very simple requirements as compared to other biological resources such as microorganisms which possess expensive requirements such as maintenance of the sterile conditions, culture media and other chemicals.[60] The phytochemical stabilization of the nanoparticles is generally considered to improve the various pharmacognostic properties of the nanoparticles. It has been well reported that phytochemically stabilized nanoparticles shows enhanced biological and physicochemical properties as compared to the nanoparticles synthesized from other routes. Previously, nano-sulfur synthesized using the extracts of *Punica granatum* revealed elevated anticancer potential as compared to the chemically synthesized nano-sulfur.[61] Similarly, in a comparative study of the chemogenic and biogenic titanium oxide nanoparticles, the biogenic titanium oxide nanoparticles revealed enhanced antibacterial properties as compared to the chemogenic.[62] Enhancement in the physical properties using biogenic synthesis has also been reported. The green synthesized silicon oxide nanoparticles using *Rhus coriaria* are reported to have enhanced stability as compared to the chemically synthesized silicon oxide nanoparticles.[63] The enhanced properties of the biogenic nanoparticles are attributed to their phytochemical stabilization which enhance surface functionalization properties and increase the physicochemical interactions.[64] In addition, the phytochemical stabilization usually includes the phenols,

flavonoids and other secondary metabolites that impart differential characteristics to the biogenic nanoparticles and enhances their efficacy.

5. Conclusion

In this work, the holmium oxide nanoparticles were biofabricated using a cost effective and green process that constituted the application of the aqueous extracts of *H. thebaica*. The nanoparticles were in the range of 6–10 nm, highly crystalline and with spherical to cuboidal morphologies. The optical bandgap (E_g) which was calculated to be 5.1 eV with major emission peaks at 415 nm and 607 nm obtained by PL spectrum. The biological response in different bioassays was dose dependent. The anticancer activities revealed that the holmium oxide was more effective against 3T3 cell lines as compared to the MCF-7. Furthermore, the nanoparticles were able to inhibit the formation of new vasculature during the in ovo CAM assay. Moderate antioxidant properties were observed. The antidiabetic potential of the holmium oxide nanoparticles revealed inhibitory potential against the enzymes involved in postprandial carbohydrate metabolism. Our findings suggest that the biological synthesis of holmium oxide nanoparticles is a suitable alternative to chemical and physical synthesis methods. Moreover, new avenues regarding the biomedical potential of the nano holmium oxide are revealed. We recommend further research on the synthesis and application of holmium oxide especially from the toxicity and nanomedicine perspective.

Data availability

The datasets used and/or analysed during the current study available from the corresponding author on reasonable request.

Conflicts of interest

Authors declare to have no conflict of interest.

Acknowledgements

References

1 L. S. de la Rosa, M. C. Portillo, M. Mora-Ramirez, V. C. Téllez, M. P. Castillo, H. J. Santiesteban, A. C. Santiago and O. P. Moreno, *Optik*, 2020, **216**, 164875.

2 S. Mortazavi-Derazkola, S. Zinatloo-Ajabshir and M. Salavati-Niasari, *Ceram. Int.*, 2015, **41**, 9593–9601.

3 H. E. A. Mohamed, A. T. Khalil, K. Hkiri, M. Ayaz, A. Usman, A. Sadiq, F. Ullah, M. A. Khan, A. Islam and M. Ovais, *Appl. Organomet. Chem.*, 2023, **37**, e7091.

4 G. Hussein, B. Balboul and G. Mekhemer, *J. Anal. Appl. Pyrolysis*, 2000, **56**, 263–272.

5 B. M. Abu-Zied and A. M. Asiri, *J. Rare Earths*, 2019, **37**, 185–192.

6 J. Kim, Z.-X. Luo, Y. Wu, X. Lu and M. Jay, *Carbon*, 2017, **117**, 92–99.

7 S. Zinatloo-Ajabshir, S. Mortazavi-Derazkola and M. Salavati-Niasari, *Int. J. Hydrogen Energy*, 2017, **42**, 15178–15188.

8 S. Zinatloo-Ajabshir, S. Mortazavi-Derazkola and M. Salavati-Niasari, *Ultrason. Sonochem.*, 2017, **39**, 452–460.

9 S. Mortazavi-Derazkola, S. Zinatloo-Ajabshir and M. Salavati-Niasari, *J. Mater. Sci.: Mater. Electron.*, 2017, **28**, 1914–1924.

10 P. Gastaldi, E. El-Khoury, M. Haddad, E. Mille, A. Dariel, T. Merrot and A. Faure, *J. Pediatr. Urol.*, 2022, **18**, 367.

11 C. Cerqueira-Coutinho, L. P. Vidal, S. R. Pinto and R. Santos-Oliveira, *Appl. Radiat. Isot.*, 2016, **112**, 27–30.

12 M. Abdusalyamova, F. Makhmudov, E. Shairmardanov, I. Kovalev, P. Fursikov, I. Khodos and Y. Shulga, *J. Alloys Compd.*, 2014, **601**, 31–37.

13 B. A. Balboul, *Powder Technol.*, 2000, **107**, 168–174.

14 L. M. d'Assuncao, I. Giolito and M. Ionashiro, *Thermochim. Acta*, 1989, **137**, 319–330.

15 V. K. Chaturvedi, B. Sharma, A. D. Tripathi, D. P. Yadav, K. R. Singh, J. Singh and R. P. Singh, *Front. Med. Technol.*, 2023, **5**.

16 A. J. Kora and R. B. Sashidhar, *J. Antibiot.*, 2015, **68**, 88–97.

17 A. T. Khalil, J. Iqbal, A. Shah, M. Z. Haque, I. Khan, M. Ayaz, I. Ahmad, S. Tasneem and H. Shah, 2021.

18 A. Shah, K. Ahmad, A. T. Khalil, F. Amin, G. Lutfullah, K. Khan, G. Shah and A. Ahmad, *Mater. Res. Express*, 2019, **6**, 125416.

19 H. E. A. Mohamed, S. Afridi, A. T. Khalil, D. Zia, Z. K. Shinwari, M. S. Dhlamini and M. Maaza, *J. Inorg. Organomet. Polym. Mater.*, 2020, **30**, 3241–3254.

20 H. E. A. Mohamed, S. Afridi, A. T. Khalil, D. Zia, J. Iqbal, I. Ullah, Z. K. Shinwari and M. Maaza, *Mater. Res. Express*, 2019, **6**, 1050c1059.

21 H. E. A. Mohamed, S. Afridi, A. T. Khalil, M. Ali, T. Zohra, R. Akhtar, A. Ikram, Z. K. Shinwari and M. Maaza, *Nanomedicine*, 2020, **15**, 467–488.

22 H. E. A. Mohamed, S. Afridi, A. T. Khalil, M. Ali, T. Zohra, M. Salman, A. Ikram, Z. K. Shinwari and M. Maaza, *Mater. Sci. Eng., C*, 2020, **112**, 110890.

23 H. E. Ahmed Mohamed, S. Afridi, A. T. Khalil, T. Zohra, M. Ali, M. M. Alam, A. Ikram, Z. K. Shinwari and M. Maaza, *Nanomedicine*, 2020, **15**, 1653–1669.

24 H. E. A. Mohamed, S. Afridi, A. T. Khalil, T. Zohra, M. M. Alam, A. Ikram, Z. K. Shinwari and M. Maaza, *AMB Express*, 2019, **9**, 1–14.

25 M. Q. Nasar, M. Shah, A. T. Khalil, M. Q. Kakar, M. Ayaz, A. S. Dablool and Z. K. Shinwari, *Inorg. Chem. Commun.*, 2022, **137**, 109252.

26 A. Sani, D. Hassan, A. T. Khalil, A. Mughal, A. El-Mallul, M. Ayaz, Z. Yessimbekov, Z. K. Shinwari and M. Maaza, *J. Biomol. Struct. Dyn.*, 2021, **39**, 4133–4147.

27 A. T. Khalil, M. Ayaz, M. Ovais, A. Wadood, M. Ali, Z. K. Shinwari and M. Maaza, *Inorg. Nano-Met. Chem.*, 2018, **48**, 441–448.

28 A. K. Zak, W. A. Majid, M. E. Abrishami and R. Yousefi, *Solid State Sci.*, 2011, **13**, 251–256.

29 P. Bindu and S. Thomas, *J. Theor. Appl. Phys.*, 2014, **8**, 123–134.

30 S. M. Shah, M. Ayaz, A.-u. Khan, F. Ullah, K. Farhan, A.-u.-H. A. Shah, H. Iqbal and S. Hussain, *Toxicol. Ind. Health*, 2015, **31**, 1037–1043.

31 A. T. Khalil, M. D. Khan, S. Razzaque, S. Afridi, I. Ullah, J. Iqbal, S. Tasneem, A. Shah, Z. K. Shinwari and N. Revaprasadu, *Appl. Nanosci.*, 2021, **11**, 2489–2502.

32 M. Ghufran, A. U. Rehman, M. Ayaz, Z. Ul-Haq, R. Uddin, S. S. Azam and A. Wadood, *J. Biomol. Struct. Dyn.*, 2022, 1–15.

33 S. Ahmad, F. Ullah, M. Ayaz, A. Zeb, F. Ullah and A. Sadiq, *Biol. Res.*, 2016, **49**, 1–9.

34 T. Kanwal, M. Kawish, R. Maharjan, I. Ghaffar, H. S. Ali, M. Imran, S. Perveen, S. Saifullah, S. U. Simjee and M. R. Shah, *J. Mol. Liq.*, 2019, **289**, 111098.

35 H. Rehman, W. Ali, M. Ali, N. Z. Khan, M. Aasim, A. A. Khan, T. Khan, M. Ali, A. Ali and M. Ayaz, *PLoS One*, 2023, **18**, e0280553.

36 F. Hussain, Z. Khan, M. S. Jan, S. Ahmad, A. Ahmad, U. Rashid, F. Ullah, M. Ayaz and A. Sadiq, *Bioorg. Chem.*, 2019, **91**, 103128.

37 M. H. Mahnashi, Y. S. Alqahtani, B. A. Alyami, A. O. Alqarni, S. A. Alqahl, F. Ullah, A. Sadiq, A. Zeb, M. Ghufran and A. Kuraev, *BMC Complementary Med. Ther.*, 2022, **22**, 26.

38 S. Manjunatha, T. Machappa, Y. Ravikiran, B. Chethan and M. Revanasiddappa, *Appl. Phys. A: Mater. Sci. Process.*, 2019, **125**, 1–10.

39 Y. Jinqiu, C. Lei, H. Huaqiang, Y. Shihong, H. Yunsheng and W. Hao, *J. Rare Earths*, 2014, **32**, 1–4.

40 N. Dilawar, S. Mehrotra, D. Varandani, B. Kumaraswamy, S. Haldar and A. Bandyopadhyay, *Mater. Charact.*, 2008, **59**, 462–467.

41 T. Wiktorczyk, *Thin Solid Films*, 2002, **405**, 238–242.

42 S. R. Alizadeh, M. Seyedabadi, M. Montazeri, B. A. Khan and M. A. Ebrahimzadeh, *Mater. Chem. Phys.*, 2023, **296**, 127240.

43 E. R. Camelo, J. D. S. Castro and C. F. das Virgens, *J. Therm. Anal. Calorim.*, 2023, **148**, 49–62.

44 L. Wu, G. Huang, T. Xie, A. Zhang and Y. Fu, *Colloids Surf., A*, 2023, **658**, 130773.

45 H. E. A. Mohamed, S. Afridi, A. T. Khalil, T. Zohra, M. M. Alam, A. Ikram, Z. K. Shinwari and M. Maaza, *AMB Express*, 2019, **9**, 1–14.

46 H. E. A. Mohamed, S. Afridi, A. T. Khalil, D. Zia, Z. K. Shinwari, M. S. Dhlamini and M. Maaza, *J. Inorg. Organomet. Polym. Mater.*, 2020, **30**, 3241–3254.

47 H. Mohamed, T. Thema and M. Dhlamini, *Mater. Today: Proc.*, 2021, **36**, 591–594.

48 H. E. A. Mohamed, A. T. Khalil, K. Hkiri, M. Ayaz, J. A. Abbasi, A. Sadiq, F. Ullah, A. Nawaz, I. Ullah and M. Maaza, *AMB Express*, 2023, **13**, 24.

49 A. N. A. Rahman, M. A. AbdelMageed, M. E. M. Assayed, H. S. A.-R. Gharib, M. A. Nasr, G. E. Elshopakey, H. A. Moniem, S. E. Shahin, E. ELHusseiny and S. A. Ahmed, *Aquaculture*, 2023, **564**, 739058.

50 F. R. Saber, S. H. Aly, M. A. Khallaf, H. A. El-Nashar, N. M. Fahmy, M. El-Shazly, R. Radha, S. Prakash, M. Kumar and D. Taha, *Food Anal. Methods*, 2022, 1–21.

51 A. Pridyantari, A. Ningrum, W. Handayani and C. Imawan, 2020.

52 K. Shinde, W. Nan, M. Tien, H. Lin, H.-R. Park, S.-C. Yu, K. Chung and D.-H. Kim, *J. Magn. Magn. Mater.*, 2020, **500**, 166391.

53 K. Kaliyamoorthi, S. Ramasamy, A. S. Pillai, A. Alexander, A. Arivarasu and I. V. Enoch, *Mater. Lett.*, 2021, **285**, 129164.

54 Y. Zeng, H. Chen, F. Yang, H. Li and P. Yang, *Mater. Res. Express*, 2022, **9**, 115011.

55 N. S. Chundawat, S. Jadoun, P. Zarrintaj and N. P. S. Chauhan, *Polyhedron*, 2021, **207**, 115387.

56 M. Ghufran, A. U. Rehman, M. Shah, M. Ayaz, H. L. Ng and A. Wadood, *J. Biomol. Struct. Dyn.*, 2020, **38**, 5488–5499.

57 M. Ghufran, H. A. Khan, M. Ullah, S. Ghufran, M. Ayaz, M. Siddiq, S. S. u. Hassan and S. Bungau, *Cancers*, 2022, **14**, 4884.

58 M. H. Mahnashi, Y. S. Alqahtani, B. A. Alyami, A. O. Alqarni, F. Ullah, A. Wadood, A. Sadiq, A. Shareef and M. Ayaz, *BMC Complementary Med. Ther.*, 2021, **21**, 1–14.

59 H. Gin and V. Rigalleau, *Diabetes Metab.*, 2000, **26**, 265–272.

60 N. S. Hamed, E. F. Taha and S. Khateeb, *Cell Biochem. Funct.*, 2023, 1–18.

61 S. Krishnappa, C. M. Naganna, H. K. Rajan, S. Rajashekarappa and H. B. Gowdru, *ACS Omega*, 2021, **6**, 32548–32562.

62 S. M. Hunagund, V. R. Desai, J. S. Kadadevarmath, D. A. Barretto, S. Vootla and A. H. Sidarai, *RSC Adv.*, 2016, **6**, 97438–97444.

63 C. Y. Rahimzadeh, A. A. Barzinjy, A. S. Mohammed and S. M. Hamad, *PLoS One*, 2022, **17**, e0268184.

64 N. T. T. Nguyen, L. M. Nguyen, T. T. T. Nguyen, T. T. Nguyen, D. T. C. Nguyen and T. V. Tran, *Environ. Chem. Lett.*, 2022, **20**, 2531–2571.